Full length article

Microstructural evolution and strain-hardening in TWIP Ti alloys

Guo-Hua Zhao[a], Xin Xu[b], David Dye[b], Pedro E.J. Rivera-Díaz-del-Castillo[a,*]

[a] *Department of Engineering, Lancaster University, LA1 4YK Lancaster, UK*
[b] *Department of Materials, Imperial College London, London SW7 2AZ, UK*

A B S T R A C T

A multiscale dislocation-based model was built to describe, for the first time, the microstructural evolution and strain-hardening of $\{332\}\langle113\rangle$ TWIP (twinning-induced plasticity) Ti alloys. This model not only incorporates the reduced dislocation mean free path by emerging twin obstacles, but also quantifies the internal stress fields present at β-matrix/twin interfaces. The model was validated with the novel Ti-11Mo-5Sn-5Nb alloy (wt.%), as well as an extensive series of alloys undergoing $\{332\}\langle113\rangle$ twinning at various deformation conditions. The quantitative model revealed that solid solution hardening is the main contributor to the yield stress, where multicomponent alloys or alloys containing eutectoid β-stabilisers exhibited higher yield strength. The evolution of twinning volume fraction, intertwin spacing, dislocation density and flow stress were successfully described. Particular attention was devoted to investigate the effect of strain rate on the twinning kinetics and dislocation annihilation. The modelling results clarified the role of each strengthening mechanism and established the influence of phase stability on twinning enhanced strain-hardening. Strain-hardening stems from the formation of twin obstacles in early stages, whereas the internal stress fields provide a long-lasting strengthening effect throughout the plastic deformation. A tool for alloy design by controlling TWIP is presented.

© 2019 The Authors. Published by Elsevier Ltd on behalf of Acta Materialia Inc.
This is an open access article under the CC BY license (http://creativecommons.org/licenses/by/4.0/)

1. Introduction

Titanium alloys have been serving as structural materials for aerospace applications, owing to their high specific strength (strength-to-weight ratio), corrosion resistance and attractive fracture toughness (the energy required to propagate cracks [1]). The demand of environment friendly and fuel efficient aircraft calls for new structural applications of Ti alloys. Boeing 787 Dreamliner utilises 15% Ti of alloys upon structural weight, this accounts for the largest weight percentage of Ti used in civil aeroplanes to date [1]. In response to the radical B787, Airbus put forward the new A350XWB (extra wide body) where the applications of Ti alloys reach 14% by structural weight compared to 6% on A380 [2]. Similar to other metals, Ti alloys can be strengthened through the controlled creation of internal defects or interfaces that obstruct dislocation motions [3]. The strength-ductility trade-off can be effectively overcome by introducing mechanical twinning or strain-induced phase transformations, which simultaneously improve the strength and uniform elongation through significant strain-hardening. β-Ti alloys retaining the bcc (body-centred cubic) structure exhibit phase-stability-sensitive deformation modes

including strain-induced α'' martensitic transformation (orthorhombic) [4], strain-induced ω phase transformation (hexagonal or trigonal) [5], $\{332\}\langle113\rangle$ twinning [6], $\{112\}\langle111\rangle$ twinning [7] and dislocation slip [8]. In general it is believed that the required fault energy (γ_{FE}, the energy to inelastically shear the material in one-atomic-layer) to operate the different deformation modes follows: $(\gamma_{FE})_{slip} > (\gamma_{FE})_{\{112\}\langle111\rangle} > (\gamma_{FE})_{\{332\}\langle113\rangle} > (\gamma_{FE})_{\beta\rightarrow\alpha''}$ [9,10].

Mechanical twinning is a fundamental deformation mode that competes against dislocation slip in crystalline solids. $\{112\}\langle111\rangle$ is a common twinning system in both bcc and fcc (face-centred cubic) metals where atoms shear along closely packed planes and directions. However, $\{332\}\langle113\rangle$ is unique as the most operative twinning system in metastable bcc Ti alloys. Crocker [11] introduced a fundamental crystallographic model and comparatively investigated both {112} and {332} twinning systems. He pointed out that pure shear occurs in $\{112\}\langle111\rangle$ twins with a magnitude of $1/\sqrt{2}$ where no atomic shuffling happens. On the other hand, $\{332\}\langle113\rangle$ twinning can only move one-half of the atoms from the untwinned lattice sites with an associated shear strain of $1/(2\sqrt{2})$, so that additional shuffling is necessary to transport the rest of the atoms to their correct positions. Tobe *et al.* [12] suggested that the decreased β-stability in metastable Ti alloys causes a lower shear modulus $c' = (c_{11} - c_{12})/2$, where c_{ij} represents each elastic

---

* Corresponding author.
  E-mail address: p.rivera1@lancaster.ac.uk (P.E.J. Rivera-Díaz-del-Castillo).

stiffness component in cubic symmetry [13]. They found that lattice instability makes {112}⟨111⟩ twinning unlikely to operate because the lattice modulation induced extra shuffling for such twinning, and therefore {332}⟨113⟩ twining turned to be energetically favourable.

TWIP effect provides delayed necking in tension through accommodative twinning shear, which is especially important for bcc Ti alloys because they display negligible uniform elongation when deformation is operated by only dislocation slip [14]. There has been a number of physics-based models attempting to describe TWIP effects in fcc metals [15]. Rémy investigated the growth of twin volume fractions and the critical strain for twin formation in low-SFE (stacking fault energy) Co-Ni alloys [16]. He presented the first model on {112}⟨111⟩ twin nuclei by considering a three-layer microtwin mechanism. Two perfect dislocations split into fault pairs and react on the primary slip plane to produce three Shockley partial dislocations on adjacent planes via the reaction: $\frac{1}{2}\langle 110\rangle + \frac{1}{2}\langle 101\rangle \rightarrow 3 \times \frac{1}{6}\langle 211\rangle$. Bouaziz introduced the well-known dynamic Hall–Petch effect in TWIP steels, where the dislocation mean free path is significantly reduced due to the emergence of obstructive twin boundaries [17]. Later the effect of backstress was introduced as dislocation pile-up contributes kinematic hardening [18]. Recently, Galindo-Nava and Rivera-Díaz-del-Castillo [19] reported a dislocation-based model particularly considering the nucleation and growth mechanisms of {112}⟨111⟩ twins and TRIP (transformation-induced plasticity) effect in austenitic steels. The operation range of deformation twinning and martensitic transformation in different strain levels was related to stacking fault energy. In the past decades, {112} twinning mechanisms have been well explored in TWIP steels [20], however the nucleation and kinetics of the {332} twinning in Ti alloys are quite different from the partial dislocation dissociation mechanism. It makes the established twinning models in fcc steels hard to be applied to bcc Ti alloys. To the best of the authors knowledge, at present no strain-hardening model has been reported for {332}⟨113⟩ TWIP Ti alloys.

The objective of this work is to introduce a dislocation-based modelling approach to quantitatively evaluate the strengthening mechanisms, as well as to describe the microstructural evolution and strain-hardening in TWIP Ti alloys. The model incorporates (i) isotropic hardening through the growth of dislocation forest; (ii) dynamic grain refinement by emerging of twin obstacles and (iii) internal stress fields induced by kinematic hardening. The paper is structured as follows: Section 2 presents a review of empirical approaches that connect alloy compositions and deformation modes via electronic structure concepts. In Section 3, a new quaternary Ti-11Mo-5Sn-5Nb alloy is produced and experimentally investigated in terms of the mechanical properties and deformation microstructure. An integral constitutive model embedding twinning kinetics is developed in Section 4. The model was validated with a large dataset of TWIP Ti alloys in Section 5. In Section 6, the overall constitutive modelling approach is outlined, and the effect of strain rate and intrinsic phase stability on strain-hardening is discussed. Concluding remarks are presented in Section 7.

2. An integral approach to composition, deformation mode and mechanical properties

Morinaga proposed an alloy design approach based on molecular orbital calculations [21,22]. Two key parameters, bond order (Bo) and metal d-orbital energy level (Md), were calculated and further linked to phase stability. Bo exhibits the electron cloud overlap between solute and solvent, which is a measurement of the covalent bond strength between the alloying elements and the matrix. Md correlates with the electronegativity and atomic radii of the solutes. The average value $\overline{Bo}$ and $\overline{Md}$ can be simply computed by taking the compositional average: $\overline{Bo} = \sum (Bo)_i X_i$ and
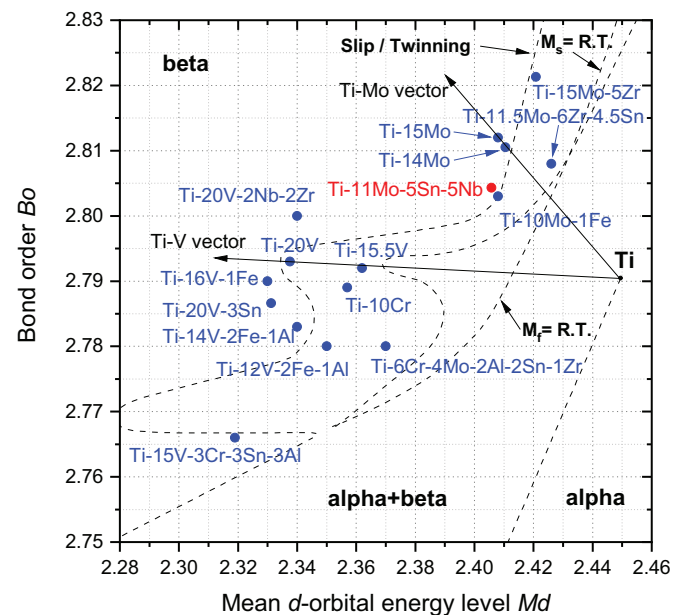

Fig. 1. TWIP Ti alloys and their locations on the so-called $Bo - Md$ map. $M_s = R.T.$ and $M_f = R.T.$ refer to martensitic transformation starting temperature equals to room temperature and transformation finishing temperature equals to room temperature, respectively. The empirical borders (dashed curves) i.e. $slip/twinning$, $M_s = R.T.$, $M_f = R.T.$ and phase boundary are extracted from Morinaga et al. [21].

$\overline{Md} = \sum (Md)_i X_i$, where X_i is the atomic percent of i solute. Empirical borders in Fig. 1 not only divide α, $\alpha + \beta$ and β phase regions, but also aid in distinguishing different deformation modes ($slip/twinning$, $M_s = R.T.$ and $M_f = R.T.$). This diagram has been extensively utilised to produce alloys with desired TWIP or combined TWIP/TRIP effects [4].

The electronic parameters of TWIP Ti alloys [23–30] were calculated and the alloy compositions are located in the $Bo - Md$ map in Fig. 1. The parameters are only composition dependent, whereas the alloy processing conditions are not reflected. Most of TWIP alloys agree with the empirical borders in Fig. 1, locating them in the $twinning$ area. Nevertheless, it is interesting to witness that some alloys violate the boundary constraints and locate in the $slip$ region. Such phenomena indicate that the empirical borders may not be accurate guidelines for TWIP/TRIP alloy design. Yet the $Bo - Md$ map still provides a visual aid to demonstrate the effect of each alloying element on the transition between deformation modes.

Tensile stress-strain curves of TWIP alloys are replotted in one single graph (Fig. 2) for clear comparison. The corresponding source to each curve is shown in Table 1. {332}⟨113⟩ is the dominant twinning mode for all documented alloys. Although strain-induced $\beta \rightarrow \omega$ transformation is observed in some of the Ti-V and Ti-Cr based alloys, ω phase transformation is known to have a marginal contribution to strain-hardening [4]. A significant advantage of TWIP Ti alloys compared to the TRIP/TWIP ones is that the yield strength of the former can easily achieve over 600 MPa with controlled grain size and solid solution hardening, whilst preserving excellent ductility and ultimate strength. It is useful to comparatively study the alloy compositions with their deformation mode referring to $Bo - Md$ map and their mechanical properties.

3. Experimental results

3.1. Materials and experimental procedure

A new quaternary Ti-11Mo-5Sn-5Nb alloy (wt.%) is proposed in this work. Its location on the $Bo - Md$ map is highlighted in Fig. 1. The as-cast ingot with a cross-sectional area of 23×23 mm^2
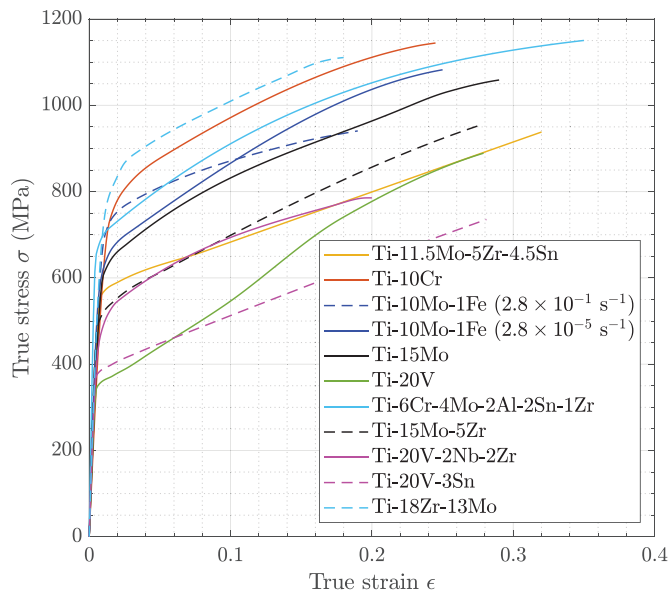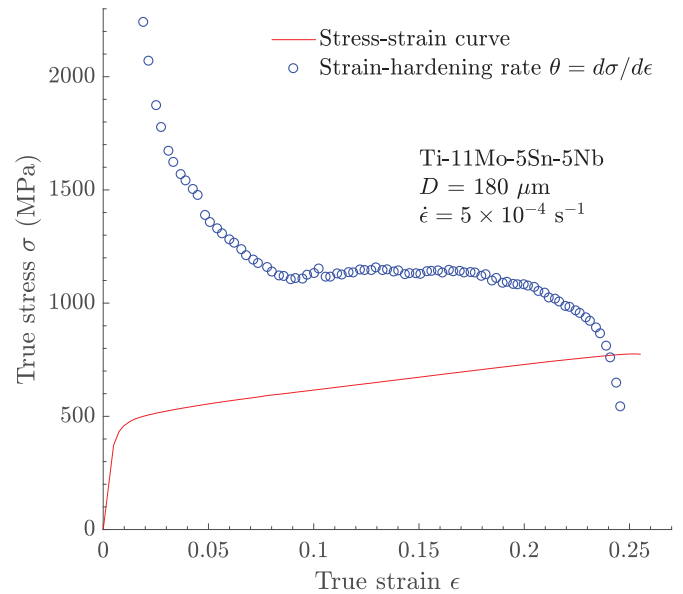
Fig. 2. Tensile stress-strain curves of TWIP Ti alloys at room temperature [23,24,26,28–30,32]. The yield stress can achieve over 600 MPa with controlled grain size and solid solution hardening. Meanwhile excellent plastic elongation (> 20%) can be preserved through significant strain-hardening (300 – 450 MPa).

Fig. 3. Tensile stress-strain curve of the Ti-11Mo-5Sn-5Nb alloy and the corresponding strain-hardening rate curve ($\theta = d\sigma/d\epsilon$). It shows excellent uniform elongation via twinning-induced strain-hardening.

was hot shape-rolled in the β-phase field (900 °C) to a bar with a cross-section area of 13×13 mm^2. Then the bar was solution-treated at 900 °C for 30 min followed by water quenching. Tensile samples with gauge dimensions of $1.5 \times 1.5 \times 19$ mm^3 were machined and polished in the as-solution-treated state. Tensile tests were performed along the rolling direction with an extensometer, under a constant strain rate $\dot{\epsilon} = 5 \times 10^{-4}$ s^{-1}. Electron backscatter diffraction (EBSD) was performed on a ZEISS Sigma scanning electron microscope (SEM). Bruker QUANTAX software was used to acquire and post-process data. The gauge and the tab/gauge connecting areas were characterised comparatively to reveal the twinning formation in different strain levels. In both areas the total map size is 286.4×214.8 µm^2 and the scanning step size is 0.6 µm. The undeformed tab area was also observed in EBSD for obtaining the average grain size. The total map size in the tab area is 1909×1432 µm^2 and the scanning step size is 3 µm. 159 grains were scanned in the tab area, and the average grain size is 139 µm with a standard deviation of 76 µm. Both microscope working distance and detector-to-sample distance are around 15 mm. 100–140 pixels were used to calculate the pole figures. EBSD maps were post-processed, grains containing less than five pixels were removed and the zero solution pixels were filled with an average value of their surrounding pixels.

3.2. Mechanical properties and microstructure

Fig. 3 shows the stress-strain curve and the corresponding strain-hardening rate ($\theta = d\sigma/d\epsilon$) of Ti-11Mo-5Sn-5Nb. The yield stress and ultimate tensile stress were 490 MPa and 788 MPa, respectively, where necking initiated at 24% strain. A typical strain-hardening rate curve of TWIP alloys was exhibited, i.e. a long steady plateau in the intermediate stage (10% – 20% strain) of deformation. In contrast with this, Ti alloys with combined TWIP/TRIP effects usually exhibit a much higher strain-hardening rate [31,33], which increases from early stages and achieves a maximum value at intermediate strains. The increased strain-hardening rate in TWIP/TRIP alloys is caused by the simultaneous activation of mechanical twinning and martensitic transformation, where the primary α'' martensite may produce extra barriers to obstruct dis-

location motions [33]. Therefore the TWIP and TWIP/TRIP alloys behave differently in terms of strain-hardening rate.

Fig. 4 displays EBSD maps at different regions of a specimen deformed until fracture (26% strain). The nearly unstrained microstructure at the tab/gauge connecting area (Fig. 4a and b) was captured, where a small amount of thin twinning bands were activated in some of the grains. At the heavily stained gauge area, thickened and dense twining bands took shape (Fig. 4c and d). Twins were transferred through neighbouring grain boundaries and became nucleation spots for new twins due to the localised stress concentrations. The increased number of twins promoted the twinning area fraction to over 50%. In next section, an integral model is developed to describe the dynamically refined microstructure by twinning and the enhanced strain-hardening.

4. Model development

4.1. Evolution of microstructure and dislocation density

Prescribing the multiplication of dislocation density is necessary for investigating the evolution of twin volume fraction and flow stress. Dislocation activity in the β-matrix is affected when the twinning volume fraction f_{tw} increases to accommodate extra strain. The total macroscopic strain increment $d\epsilon$ can be described using a rule of mixtures incorporating twinning and dislocation slip contributions:

$$d\epsilon = (1 - f_{tw})\, d\epsilon_{dis} + \epsilon_{tw}\, df_{tw} \qquad (1)$$

where $d\epsilon_{dis}$ is the strain increment in the untwinned β-matrix undergoing dislocation slip and df_{tw} is the increment in twinning volume fraction. The Taylor factor M is used to describe an average texture orientation in the isotropic model, which depends on the crystallographic nature of the assumed slip or twinning system. $M = 2.8$ was calculated for bcc metals [34]. Thereafter the relationship between macroscopic strain and shear strain is expressed as: $\epsilon = \gamma/M$. The shear strain of {332}⟨113⟩ twinning is $\gamma_{tw} = 1/(2\sqrt{2})$ where one-half atoms are rearranged by shuffling. Thus Eq. (1) becomes
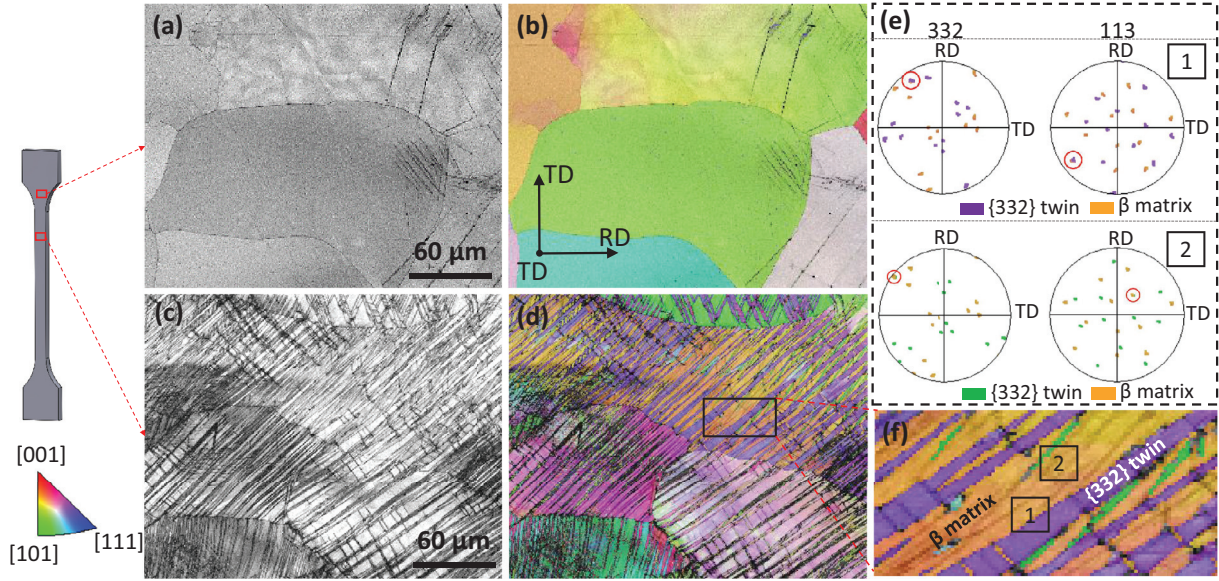
Fig. 4. (a) EBSD pattern quality map and (b) Inverse pole figure (IPF) at tab/gauge connecting area of the deformed (26% strain) Ti-11Mo-5Sn-5Nb, where thin deformation twins are visible. (c) Pattern quality map and (d) IPF in the gauge area, showing heavily deformed microstructure with dense twinning bands. (e) Pole figures of {332}⟨113⟩ twinning corresponding to the detected areas in (f) the enlarged twinning zone.

$$\frac{d\epsilon_{dis}}{d\epsilon} = \frac{1}{1-f_{tw}}\left(1 - \frac{1}{2\sqrt{2}M}\frac{df_{tw}}{d\epsilon}\right) \tag{2}$$

The evolution of dislocation density ρ as a function of macroscopic strain can be expressed as:

$$\frac{d\rho}{d\epsilon} = \frac{d\rho}{d\epsilon_{dis}}\frac{d\epsilon_{dis}}{d\epsilon} = \frac{d\rho}{d\epsilon_{dis}}\frac{1}{1-f_{tw}}\left(1 - \frac{1}{2\sqrt{2}M}\frac{df_{tw}}{d\epsilon}\right) \tag{3}$$

where $d\rho/d\epsilon_{dis}$ represents the evolution of dislocation density in the untwined β-matrix. It results from the competition between dislocation accumulation $d\rho^+/d\epsilon_{dis}$ and annihilation $d\rho^-/d\epsilon_{dis}$ due to dynamic recovery [19]. The dislocation storage term incorporates contributions from (i) the dislocation forest induced by dislocation interactions; (ii) the dislocation impedance by grain boundaries; and (iii) the dynamically decreased intertwin spacing L (Fig. 5a). Deformation twins can be regarded as thin circular disks according to the stereological relationship built by the Fullman's volumetric analysis [16]. If N_L is the number of twin intersected by any line per unit length, one obtains:

$$\frac{1}{L} = \frac{1}{2t}\frac{f_{tw}}{1-f_{tw}} \tag{4}$$

where t is the mean twin thickness.

The dislocation mean free path Λ is the distance travelled by a dislocation segment before it is stopped by the interaction with microstructural features such as other dislocations (in a forest), grain boundaries and β-matrix/twin interfaces. Their relationship can be expressed as a harmonic mean:

$$\frac{1}{\Lambda} = k\sqrt{\rho} + \frac{1}{D} + \frac{1}{L} \tag{5}$$

where k is a dislocation storage coefficient. The incremental dislocation storage rate $d\rho^+/d\epsilon_{dis} = Mb/\Lambda$, where b is the magnitude of the Burgers vector. Thus the evolution of the dislocation density in the β-matrix facilitated by dislocation slip is given by:

$$\frac{d\rho}{d\epsilon_{dis}} = \frac{d\rho^+}{d\epsilon_{dis}} - \frac{d\rho^-}{d\epsilon_{dis}} = M\left(\frac{k}{b}\sqrt{\rho} + \frac{1}{bD} + \frac{1}{2tb}\frac{f_{tw}}{1-f_{tw}} - f_{DRV}\rho\right) \tag{6}$$

where f_{DRV} is the dynamic recovery coefficient and the $(f_{DRV}\rho)$ term accounts for dislocation annihilation.
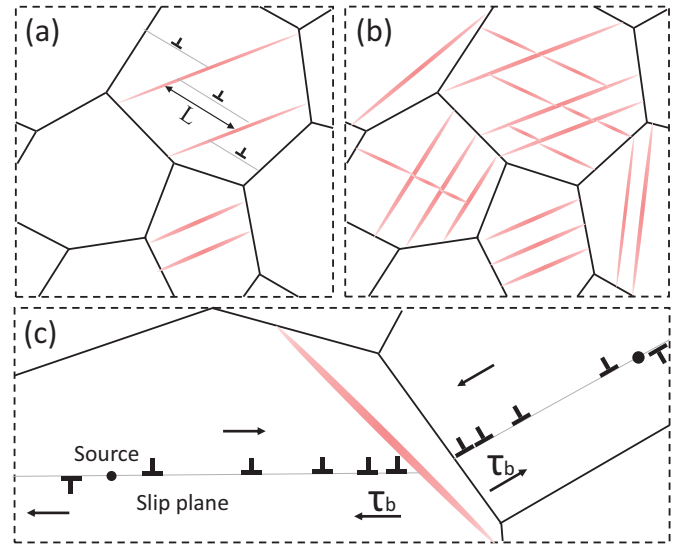
Fig. 5. Schematic representation of the strain-hardening mechanisms in TWIP Ti alloys. (a) {332}⟨113⟩ twins form at the onset of critical strain for twin nucleation ϵ_T. Dislocations travel along certain slip planes between obstructive intertwin spacing L. (b) Dislocation mean free path Λ is continuously reduced due to the combined effects of dynamic grain refinement and the increased dislocation forest. (c) Dislocations pile-up at twin and grain boundaries causing the building up of internal stress fields (kinematic hardening).

Twinning kinetics $df_{tw}/d\epsilon$ in Eq. (2) is a key factor representing the growing rate of twin volume fraction. Olson and Cohen [35] described the kinetics of strain-induced martensitic nucleation in austenitic steels by using a simple shear band model $df_{sb}/(1-f_{sb}) = \alpha_0 d\epsilon$, where f_{sb} is the shear bands volume fraction and α_0 represents its formation rate at low strains. This mechanism was further derived to describe the twinning kinetics in TWIP steels by Bouaziz [17,18], which expresses the evolution of twin fraction as a function of strain:

$$f_{tw} = F_0\left\{1 - \exp\left[-\beta_0(\epsilon - \epsilon_T)\right]\right\}^m \tag{7}$$

where F_0 is the maximum twin fraction, m is a fixed exponent and ϵ_T is the critical strain at the onset of twinning. β_0 is the twinning

kinetics parameter which increases at higher strain rate and with lower β stability. Upon differentiating Eq. (7), the twinning kinetics $df_{tw}/d\epsilon$ becomes:

$$\frac{df_{tw}}{d\epsilon} = F_0\,\beta_0\,m \exp\left[-\beta_0(\epsilon-\epsilon_T)\right]\left\{1-\exp\left[-\beta_0(\epsilon-\epsilon_T)\right]\right\}^{(m-1)} \tag{8}$$

It not only governs the microstructural evolution in early stages of deformation, but also further influences kinematic hardening and the flow stress response.

4.2. Kinematic hardening at β-matrix/twin interfaces

Dislocations are obstructed at coherent β-matrix/twin interfaces causing internal stress fields (backstress) to further impede the progress of slip. Conventionally the backstress by dislocation pile-ups at grain boundaries is expressed as: $\sigma_b = M\mu bn/D$, where μ is the shear modulus and n is the number of dislocations stopped at grain boundaries on a given slip plane [36]. Thereafter the backstress in TWIP alloys becomes:

$$\sigma_T = M\mu b\left(\frac{1}{L}+\frac{1}{D}\right)n \tag{9}$$

where the harmonic mean $(1/L+1/D)$ takes into account dislocation pile-ups at both twin and grain boundaries. The flux of dislocations arriving at interfaces per slip plane in the untwinned β-matrix is:

$$\frac{dn}{d\epsilon_{dis}} = M\frac{\lambda}{b}\left(1-\frac{n}{n^*}\right) \tag{10}$$

where λ is the mean spacing between slip planes and λ/b can be interpreted as the distance between slip planes necessary to operate deformation [36]. n^* is the maximum number of dislocations that can pile-up at interfaces on a given slip plane, which determines the maximum backstress that can achieve. Combining Eq. (2) and (10), the flux of dislocations with macroscopic strain is given by:

$$\frac{dn}{d\epsilon} = \frac{dn}{d\epsilon_{dis}}\frac{d\epsilon_{dis}}{d\epsilon} = M\frac{\lambda}{b}\left(1-\frac{n}{n^*}\right)\frac{1}{1-f_{tw}}\left(1-\frac{1}{2\sqrt{2}M}\frac{df_{tw}}{d\epsilon}\right) \tag{11}$$

Fig. 5 shows a schematic representation of the strain-hardening mechanisms in the present model. Mechanical twinning nucleates at small strains, usually at the elastic stage for $\{332\}\langle113\rangle$ twins. Fig. 5a and b illustrate the dynamic grain refinement: the formation of new twin obstacles gradually reduces the dislocation mean free path, thereby enhancing dislocation storage and ensuing isotropic hardening [20]. Fig. 5c demonstrates the long-range internal stress by dislocation pile-ups. Considering a dislocation source which emits a series of dislocations under the effect of external shear stress τ, where the dislocations travel lying in the same slip plane. Eventually the leading dislocation meets barriers such as β-matrix/twin interface or grain boundary configurations so that further expansion of the dislocation loop is prevented. The dislocations then pile-up behind the leading dislocation. They interact elastically and their spacing decreases towards the front of the pile-up, which exerts a back shear stress τ_b to the source [37]. The internal stress field continuously concentrates at the gradually increased β-matrix/twin interfaces, leading to a long-term strengthening contribution to the flow stress.

4.3. Yield stress prediction and flow stress evolution

The flow stress evolution led by the increase in dislocation density can be expressed by the dislocation forest model [38]. Within this, the critical stress σ_f to destroy a dislocation junction and to remobilise the dislocation lines is proportional to $\mu b/l$,
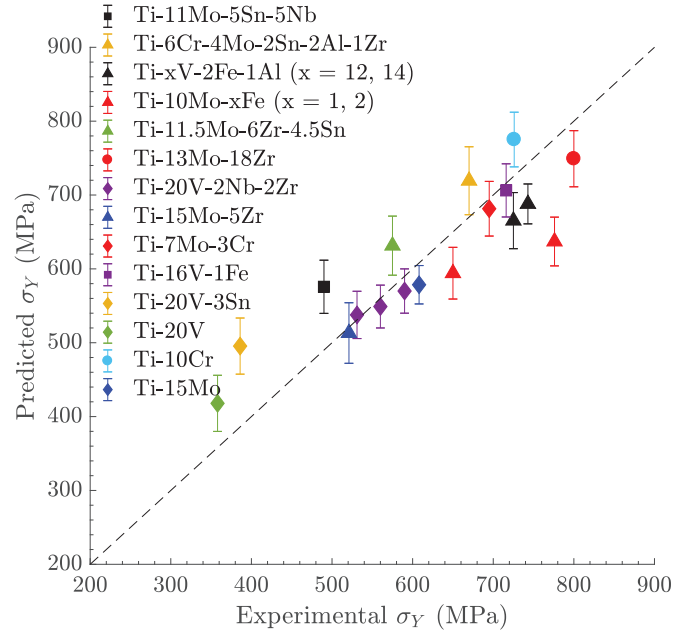

Fig. 6. Experimental *vs.* predicted yield stress for TWIP Ti alloys (Table 1). The tested alloys were deformed at room temperature under the unified strain rate (in an order of 10^{-4} s^{-1}).

where l is the distance between the intersecting obstacles along the dislocation line. Thus the average value of this distance scales as $1/\sqrt{\rho}$ and ρ is the average dislocation density. This leads to the well-known Taylor relation: $\sigma_{DF} = \alpha M\mu b\sqrt{\rho}$, where $\alpha \approx 0.3$ reflects the average strength of dislocation interactions (junction strength) over all existing configurations. Moreover, the backstress term in Eq. (9) increases as the number of pile-up dislocations n approach to the maximum value n^*. Incorporating the twinning enhanced isotropic hardening and the kinematic hardening, the flow stress evolution can be established:

$$\sigma = \sigma_0 + \alpha M\mu b\sqrt{\rho} + M\mu b\left(\frac{1}{L}+\frac{1}{D}\right)n \tag{12}$$

where σ_0 is the friction stress comprised of the critical resolved shear stress of pure Ti (τ_{CRSS}), solid solution hardening (σ_{ss}) and grain boundary strengthening (σ_{HP}):

$$\sigma_0 = \left[M\tau_{CRSS} + \left(\sum_i B_i^{3/2}X_i\right)^{2/3} + \frac{k_Y}{\sqrt{D}}\right]G(T,\dot{\epsilon}) \tag{13}$$

where X_i is the atomic fraction of solute i and B_i reflects the solid solution hardening coefficient, which accounts for shear modulus misfit and lattice parameter misfit between solvent and substitutional solutes. The value of B_i for each individual solute in multi-component Ti alloys was calculated in a recent work [34]. k_Y is the Hall–Petch coefficient of Ti alloys. $G(T,\dot{\epsilon})$ is a function of temperature and strain rate accounting for thermally activated effects altered between dislocation slip and deformation twinning. The yield stress can be calculated by: $\sigma_Y = \sigma_0 + \alpha M\mu b\sqrt{\rho_0}$, where ρ_0 reflects initial dislocation density before deformation.

5. Model validation

The model was tested against experimental data for an extensive range of TWIP Ti alloys (Table 1). Fig. 6 shows a comparison between the predicted and the measured yield stress. The alloys were deformed at room temperature under a unified strain rate (in the order of 10^{-4} s^{-1}). The yield stress predictions exhibit good agreement with the experimental data. Fig. 7 shows the

Table 1
The compositions, operative deformation modes, grain size D and strain rate $\dot{\epsilon}$ of the documented TWIP Ti alloys.

Alloy (wt.%)	Deformation modes	D (μm)	$\dot{\epsilon}$ (s^{-1})	Ref.
Ti-10Cr	{332} & $\beta \rightarrow \omega$	120	8.33×10^{-4}	[30]
Ti-7Mo-3Cr	{332} & {112}	12 – 190	4.0×10^{-4}	[31]
Ti-10Mo-1Fe	{332}	196	$2.8 \times 10^{-5} - 2.8 \times 10^{-1}$	[24]
Ti-10Mo-2Fe	Slip + {332}	200	2.78×10^{-4}	[14]
Ti-11.5Mo-6Zr-4.5Sn	{332}	200	5.2×10^{-4}	[29]
Ti-13Mo-18Zr	{332} & {112}	49	1.0×10^{-3}	[32]
Ti-15Mo	{332}	84	2.78×10^{-4}	[23]
Ti-15Mo-5Zr	{332}	200	5.2×10^{-4}	[29]
Ti-12V-2Fe-1Al	{332}	51	5.0×10^{-4}	[27]
Ti-14V-2Fe-1Al	{332}	39	5.0×10^{-4}	[27]
Ti-15.5V	{332} & $\beta \rightarrow \omega$	-	-	[25]
Ti-16V-1Fe	{332} & $\beta \rightarrow \omega$	20	5.0×10^{-4}	[27]
Ti-20V	{332} & $\beta \rightarrow \omega$	200	5.2×10^{-4}	[29]
Ti-20V-3Sn	{332}	200	5.2×10^{-4}	[29]
Ti-20V-2Nb-2Zr	{332}	8 – 28	1.0×10^{-3}	[26]
Ti-6Cr-4Mo-2Al-2Sn-1Zr	{332} & {112}	140	5.0×10^{-4}	[28]
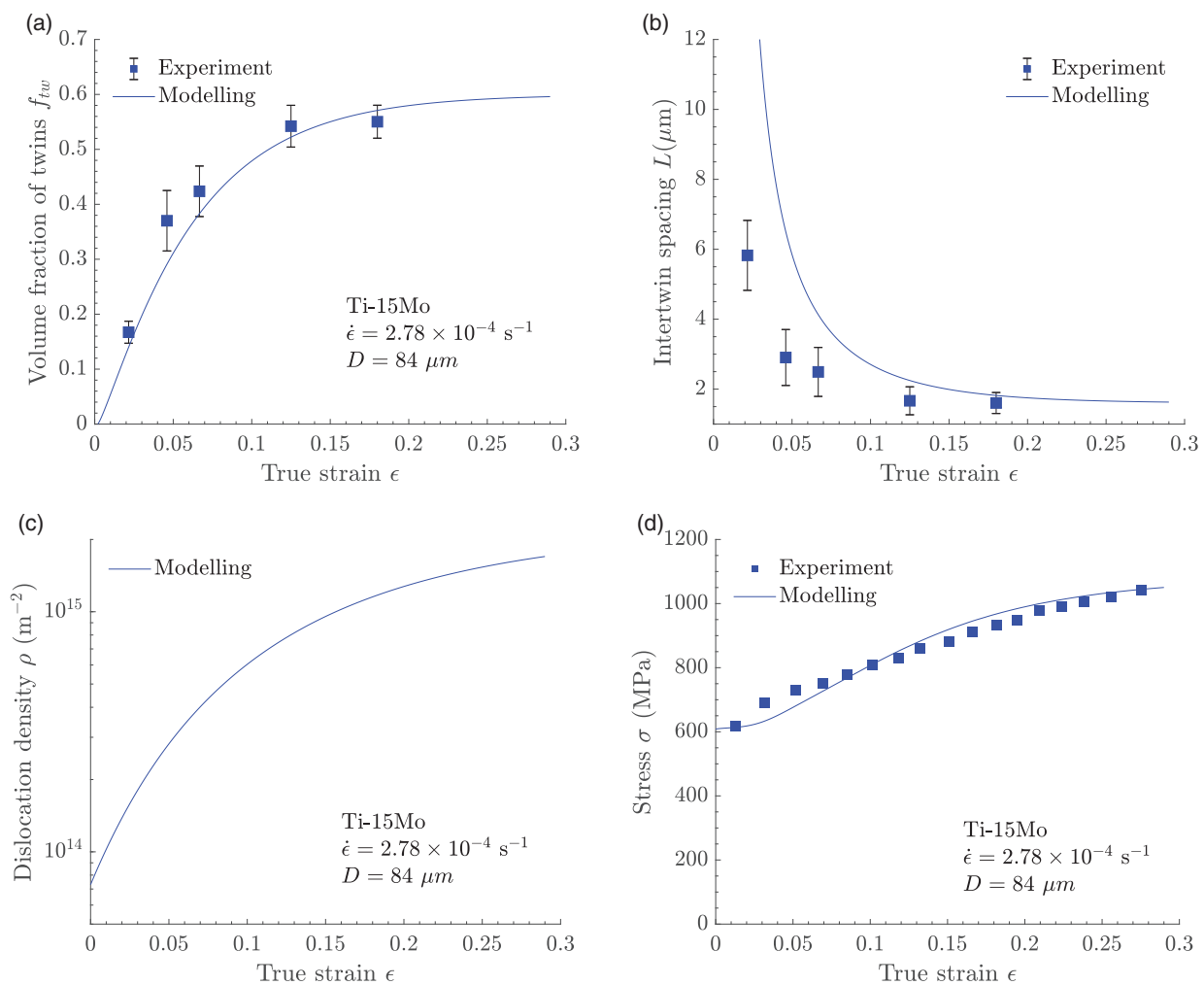
Fig. 7. Microstructure and flow stress evolution as a function of strain in Ti-15Mo. (a) The growth of twin volume fraction f_{tw} started at the onset of critical strain. (b) The reduced intertwin spacing L due to the formation of twin obstacles. (c) The average dislocation density ρ increased by twinning enhanced dislocation accumulation. (d) Macroscopic stress-strain curve showed exceptional strain-hardening.

model validation in Ti-15Mo alloy, an average twin thickness $t = 1.2\,\mu m$ was adopted from experiments [23]. The critical strain for twin nucleation ϵ_T is estimated to be 0.2% from quantitative metallography [6]. The twin volume fraction increased at the onset of critical strain (Fig. 7a), meanwhile the intertwin spacing concomitantly dropped (Fig. 7b). Both factors reached an asymptote

after 15% strain, at which more than 50% twin fraction was achieved. The evolution of dislocation density was simulated in Fig. 7c, which raised from an initial value of 7.3×10^{13} till 1.8×10^{15} m^{-2} at the point of ultimate tensile stress. The modelled flow stress well described the experimental stress-strain curve in Fig. 7d. The twin-

Table 2
Numerical values of the physical constants and of the identified parameters.

Parameter	Description	Value	Ref.
M	Taylor factor	2.8	[34]
μ	Shear modulus	39 GPa	[39]
k_Y	Hall-Petch constant	0.87 MPa·m$^{1/2}$	[34]
α	Dislocation interaction constant	0.35	[38]
b	Magnitude of Burgers vector	2.8 Å	[39]
t	Average twin thickness	1.2 μm	[23]
λ	Spacing between slip planes	150 nm	[40]
m	Exponent for twinning kinetics	1.2 ± 0.03	This work
F_0	Max twinning volume fraction	0.6 ± 0.05	This work
n^*	Max number of piled-up dislocations	8 ± 1	This work
ρ_0	Initial dislocation density	7.3 ×10^{13} m^{-2}	[24]
k	Dislocation storage coefficient	0.04 ± 0.002	This work
f_{DRV}	Dynamic recovery coefficient	4 ± 0.05	This work

[a] $F_0 = 0.5 \pm 0.04$ and $f_{DRV} = 8 \pm 0.05$ for Ti-10Mo-1Fe deformed at $\dot{\epsilon} = 2.8 \times 10^{-1}$ s^{-1}.
[b] The values of standard error associated with the identified parameters is based on the sensitivity analysis.
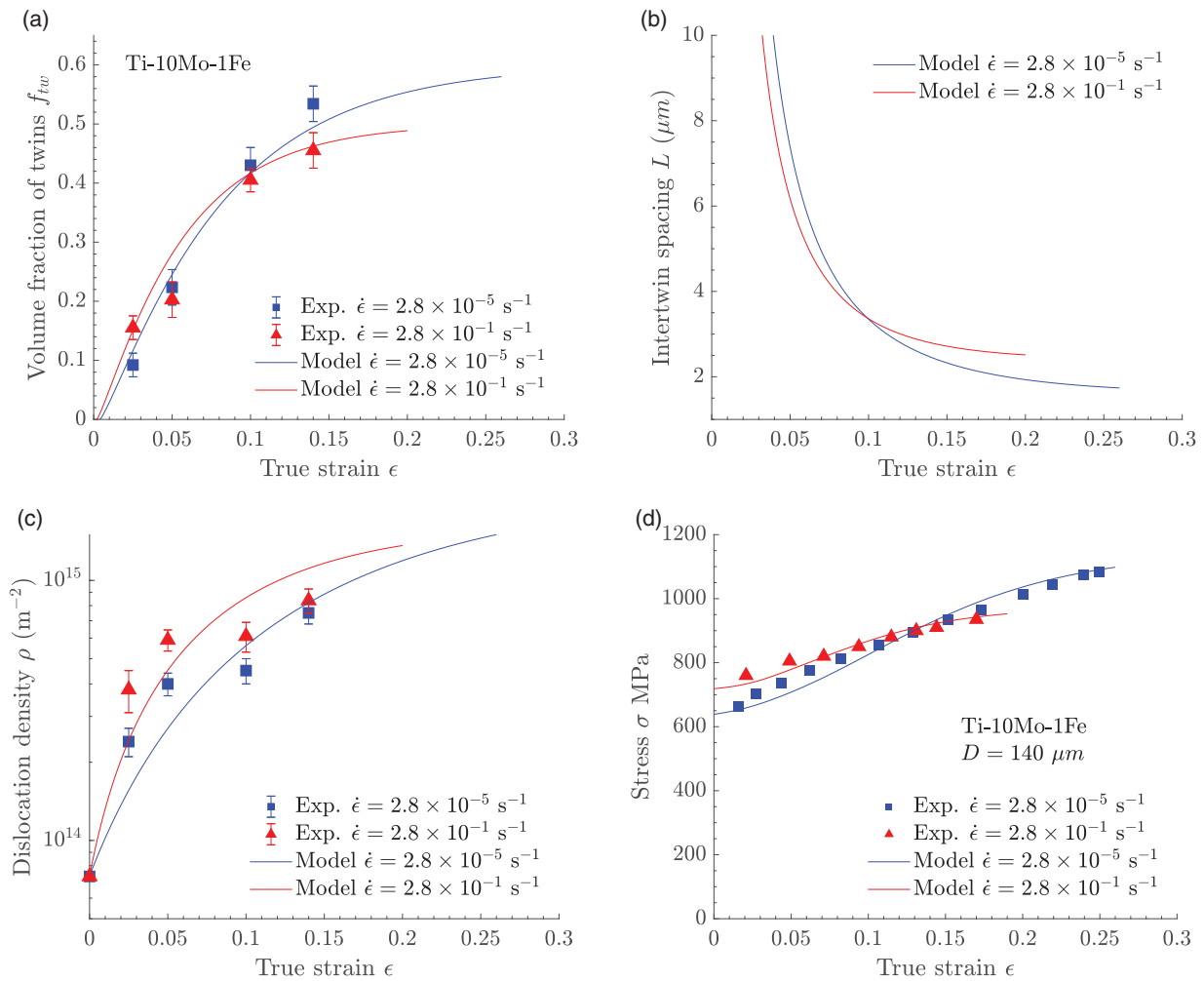
Fig. 8. Model validation in Ti-10Mo-1Fe at the strain rates of 2.8×10^{-5} and 2.8×10^{-1} s^{-1}, respectively. (a) An elevated twinning kinetics was shown at high strain rate. (b) The intertwin spacing L decreased promptly in early stages of deformation. (c) The dislocation density ρ increased faster at high strain rate due to the rapidly reduced dislocation mean free path. (d) Flow stress evolution as a function of strain.

ning kinetics parameter of Ti-15Mo is $\beta_0 = 18$ at $\dot{\epsilon} = 2.78 \times 10^{-4}$ s^{-1}. The parameters used for modelling are defined in Table 2.

Fig. 8 shows the model validation in Ti-10Mo-1Fe at low strain rate $\dot{\epsilon} = 2.8 \times 10^{-5}$ s^{-1} and high strain rate $\dot{\epsilon} = 2.8 \times 10^{-1}$ s^{-1} [24]. The alloy exhibited clear strain-rate-dependent performance. At high strain rate, both twin fraction and dislocation density in-creased significantly in early stages to accommodate the rapid deformation. However, it showed lower maximum twin fraction ($F_0 < 50\%$) and less plasticity. A high strain rate tends to promote the twin growth rate by increasing the twinning kinetics parame-ter ($\beta_0 = 20$) compared to that ($\beta_0 = 14$) at low strain rate.

The model was applied to predict the twinning evolution in a wider number of TWIP alloys such as Ti-11Mo-5Sn-5Nb,
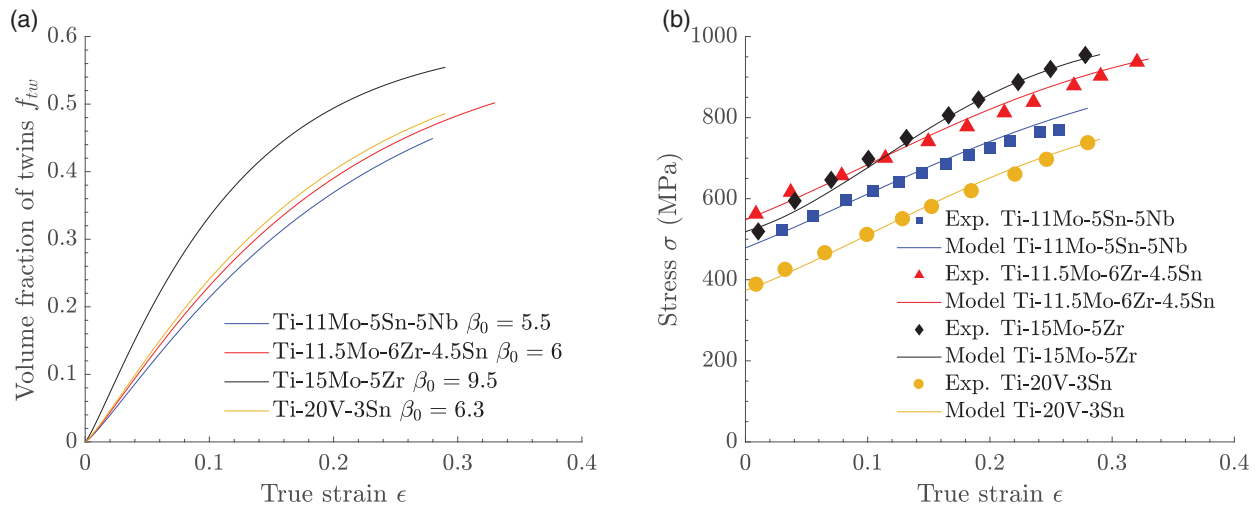
Fig. 9. (a) The predicted twinning fraction f_{tw} evolution in Ti-11Mo-5Sn-5Nb, Ti-11.5Mo-6Zr-4.5Sn, Ti-15Mo-5Zr and Ti-20V-3Sn. (b) The corresponding stress-strain behaviours which can be well reproduced by adjusting the twinning kinetics parameter β_0.
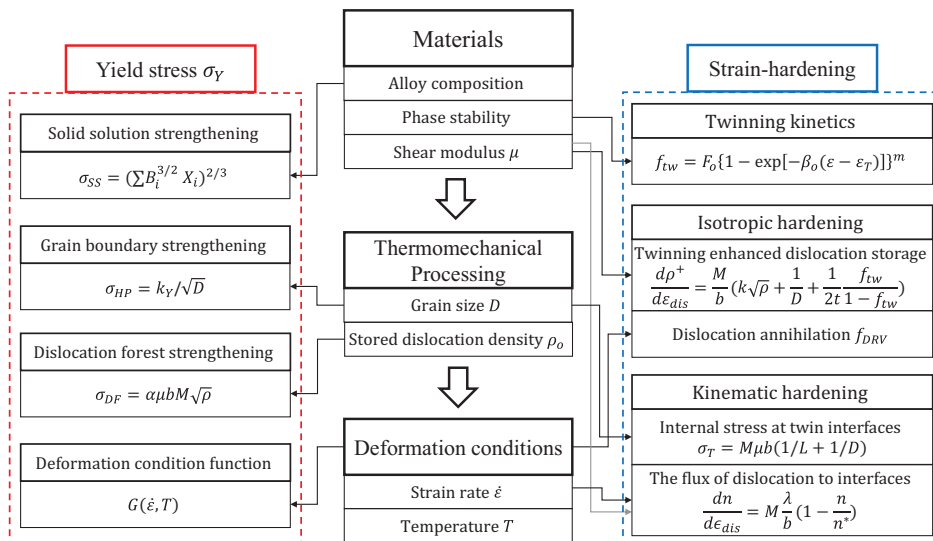
Fig. 10. Flow chart illustrating an integral modelling approach incorporating yield stress predictions and strain-hardening evolutions. The inputs include material information such as alloy composition, shear modulus, grain size and initial dislocation density, as well as deformation conditions.

Ti-11.5Mo-6Zr-4.5Sn (Beta III), Ti-15Mo-5Zr and Ti-20V-3Sn [29] in Fig. 9. Their flow stress can be well reproduced by adjusting one single variable, the twining kinetics parameter β_0. The value of β_0 for each alloy is shown in Fig. 9a and the strain-hardening is promoted as increasing β_0. Twinning kinetics is not only dependent on strain rate, but also sensitive to the alloy composition that determines the intrinsic phase stability. Less stabilised alloys display increased β_0, which is facilitated by the easy nucleation of shear bands. The model validations confirmed that macroscopic strain-hardening can be described at multiple length scales.

6. Discussion

6.1. Overview

An integral modelling approach is proposed to describe the microstructural evolution and mechanical behaviour of {332}⟨113⟩ TWIP Ti alloys. A flow chart is shown in Fig. 10 to illustrate the calculation methodology. The model is comprised of two major aspects: yield stress prediction and strain-hardening description. Input follows aspects of (i) the nature of the alloy, (ii) its processing history and (iii) the deformation conditions (centre column in Fig. 10). The solid solution hardening σ_{SS} can be quantitatively calculated from a given alloy composition. Meanwhile, the compositions plays a key role in determining β-phase stabilities which further control twinning kinetics. The grain size D and the stored dislocation density ρ_0 after thermomechanical treatments are input to calculate grain boundary strengthening σ_{HP} and dislocation forest strengthening σ_{DF}, respectively. Besides ρ_0 is fixed as initial value for modelling dislocation multiplication $d\rho/d\epsilon$. The evolution of dislocation density is a competing process between dislocation generation $d\rho^+/d\epsilon_{dis}$ and dynamic recovery $d\rho^-/d\epsilon_{dis}$. The later term is sensitive to deformation conditions e.g. strain rate and temperature, because the dislocation annihilation process is thermally activated and governed by the glide of dislocations at low and medium temperature regimes. The dislocation activities take place in the untwinned β-matrix; however, the growth of both twin fraction and dislocation forest reduce the available path for dislocations to freely glide. Moreover, internal stress fields were built at twin interfaces due to dislocation pile-ups. By aggregating

Table 3

The contributions of the solid solution hardening σ_{SSH} and the grain boundary strengthening σ_{HP} in each Ti alloy. The calculated yield stress and experimental yield stress are listed for comparison. The stress unit is MPa.

Alloy (wt.%)	σ_{SSH}	σ_{HP}	Cal. σ_Y	Exp. σ_Y
Ti-11Mo-5Sn-5Nb	226.7 ± 26.7	76.3	575.7 ± 36.3	490
Ti-6Cr-4Mo-2Al-2Sn-1Zr	300.5 ± 32.3	76.1	719.3 ± 45.7	670
Ti-12V-2Fe-1Al	166.6 ± 26.2	126.2	665.3 ± 38.3	725
Ti-14V-2Fe-1Al	171.1 ± 19.9	144.1	687.9 ± 26.9	743
Ti-10Mo-1Fe	133.6 ± 21.7	67.8	594.1 ± 35.1	652
Ti-10Mo-2Fe	177.2 ± 19.8	67.2	637.1 ± 33.6	776
Ti-11.5Mo-6Zr-4.5Sn	275.1 ± 29.7	63.6	631.4 ± 39.1	575
Ti-13Mo-18Zr	317.8 ± 25.2	128.6	749.1 ± 38	800
Ti-20V-2Nb-2Zr	123.2 ± 18.1	141.7	537.6 ± 32.2	531
Ti-15Mo-5Zr	176.8 ± 22.3	63.6	513.1 ± 40.9	521
Ti-7Mo-3Cr	182.5 ± 19.6	106.2	681.4 ± 36.9	695
Ti-16V-1Fe	132.3 ± 22.9	201.2	706.2 ± 36.5	716
Ti-20V-3Sn	169.7 ± 23.8	53.0	495.4 ± 38.3	386
Ti-20V	92.2 ± 19.6	53.0	417.9 ± 38.6	358
Ti-10Cr	341.7 ± 23.4	60.6	775.1 ± 36.7	726
Ti-15Mo	107.6 ± 16.7	98.2	578.5 ± 26.1	608

Note the yield stress of each alloy was calculated using $\sigma_Y = \sigma_0 + \alpha M \mu b \sqrt{\rho_0}$, where the expression of σ_0 is in Eq. (13). The yield stress of pure Ti is within the range of 180 – 480 MPa [42]. The contribution from dislocation forest strengthening is around 91 – 93 MPa by accounting the initial dislocation density varies in the range of $7.3 - 7.5 \times 10^{13}$ m^{-2}.

the left column in Fig. 10, the yield stress is predictable. On the other hand, flow stress evolution in the right column can be modelled by combining the twinning enhanced isotropic hardening and the internal stress field by kinematic hardening. Dislocation slip activities without twinning can be expressed using a simple Kocks–Mecking approach [41] $\frac{d\rho}{d\epsilon} = M(\frac{k}{b}\sqrt{\rho} - f_{DRV}\rho)$. In the case, the dislocation accumulation rate is the fundamental quantity for strain-hardening which only accounts for the increase in forest dislocation density. Since the bcc β-Ti alloys show poor strain-hardening in tension and negligible uniform elongation ($< 3\%$) at room temperature, the pure slip model is less appropriate for bcc Ti alloys.

6.2. Alloying contributions to yield stress and strain-hardening

The contribution of each strengthening mechanism is quantified and listed in Table 3. Most of the tested alloys were coarse grained with grain sizes in the range of 60 – 220 μm, thus the grain boundary strengthening is limited. The stored dislocation density upon quenching is around 7.5 $\times 10^{13}$ m^{-2}, which contributes to moderate strengthening by dislocation forest. The yield stress is therefore mainly enhanced by solid solution hardening. Multicomponent alloys or alloys containing eutectoid β-stabilisers, e.g. Cr or Fe, exhibited the highest SSH effects. The eutectoid elements may cause severe local lattice distortion because of the large shear modulus and lattice parameter misfit against the Ti solvent [34]. On the other hand, Ti-V based alloys display lowest SSH and yield stress due to a small shear modulus difference between V (46.7 GPa) and Ti (45.6 GPa).

Twinning kinetics $df_{tw}/d\epsilon$ is the key parameter in the present model. It is sensitive to two factors: strain rate and intrinsic phase stability of the alloy. The less stabilised alloys are more likely to activate twinning under deformation, and their twinning kinetics parameter is promoted. The strain rate affects the twinning growth and macroscopic mechanical behaviours by altering the twinning kinetics parameter β_0, the maximum twin volume fraction F_0 and the dynamic recovery coefficient f_{DRV}. The alloys deforming at high strain rate present a rapid growth of twin fraction to accommodate the fast strain increases. However, F_0 decreases at the same time and eventually fracture happens earlier. On the other hand, the plastic strain can be well accommodated by twinning for the

slowly deformed sample, where both strain energy and time are sufficient for twin nucleation and growth. The dislocation density grows significantly in early stages of fast straining due to the rapidly reduced dislocation mean free path. Nevertheless, the dynamic recovery coefficient that governs dislocation annihilation increased at a high strain rate, which had negative effects on dislocation multiplication. The strain-hardening in early stages is controlled by the formation of new twin obstacles whereas kinematic hardening keeps contributing even after a dense twinning microstructure was formed in the intermediate or late stages of deformation.

6.3. Future work

By quantitatively evaluating the strengthening mechanisms, the present model provides an efficient tool for Ti alloy design. Since this isotropic model is originally developed for understanding the effects of alloying elements on strain-hardening as well as for describing the macroscopic mechanical behaviour of polycrystalline alloys, it can hardly reflect the crystallography of isolated grains. In order to overcome this limitation, the next step is to embed the dislocation-based strain-hardening model into crystal plasticity methods or visco-plastic self-consistent (VPSC) polycrystal framework [43]. On the other hand, the nucleation and growing mechanisms of the unique {332}⟨113⟩ twinning are still unclear. An empirical expression derived from the kinetics of strain-induced martensitic nucleation was used for describing the growing of twin fraction. Even this expression well reproduced the experimental results, a physics-based function is required as we further understand the mechanisms of the {332} twinning. From the point of designing strong and ductile alloys, both superior yield strength and exceptional strain-hardening is desired. Therefore designing and modelling the TWIP Ti alloys with simultaneously activated {332}⟨113⟩ and {112}⟨111⟩ twinning would be the next natural step for future work.

7. Conclusions

1. A dislocation-based constitutive model on microstructural evolution and strain-hardening in TWIP Ti alloys has been developed. The dislocation storage term was enhanced by the formation of twin obstacles that significantly reduced the dislocation mean free path. The internal stress fields at β-matrix/twin interfaces induced by kinematic hardening further contributed to the flow stress increase.

2. The link between alloy compositions and deformation modes was built by the electronic parameters and the empirical borders. Although the $Bo - Md$ map may not be an accurate approach for alloy design, it provides a visual aid to demonstrate the effect of each alloying element on the transition between deformation modes. A new quaternary Ti-11Mo-5Sn-5Nb TWIP alloy was proposed showing excellent tensile plasticity through significant strain-hardening.

3. The model was validated with a wide range of TWIP Ti alloys, exhibiting good agreements in terms of yield stress predictions and flow stress evolutions. Solid solution hardening is the main contributor the yield stress, especially for the multicomponent alloys or the alloys containing eutectoid β-stabilisers e.g. Cr or Fe.

4. The strain-hardening and flow stress evolution can be well reproduced by adjusting twinning kinetics $df_{tw}/d\epsilon$, and this factor governs: (i) the growth rate of twin volume fraction; (ii) twinning enhanced isotropic hardening and (iii) kinematic hardening. The twinning kinetics parameter β_0 increases at high strain rate and in less stabilised alloys, which is facilitated by the easy formation of twinning shear. On the other

hand, although high strain rate promotes twinning kinetics, the dislocation annihilation becomes dominated and thereafter inhibited strain-hardening and plasticity. By quantitatively understanding the strengthening mechanisms and the origin of strain-hardening, the present work can be applied for TWIP Ti alloy design.

Declaration of Competing Interest

The authors declare that they have no known competing financial interests or personal relationships that could have appeared to influence the work reported in this paper.

Acknowledgements

References

[1] K. Lu, The future of metals, Science 328 (5976) (2010) 319–320.
[2] G. Marsh, Airbus A350 XWB update, Reinf. Plast. 54 (6) (2010) 20–24.
[3] K. Lu, L. Lu, S. Suresh, Strengthening materials by engineering coherent internal boundaries at the nanoscale, Science 324 (5925) (2009) 349–352.
[4] P. Castany, T. Gloriant, F. Sun, P. Prima, Design of strain-transformable titanium alloys, C.R. Phys. 19 (8) (2018) 710–720.
[5] J. Zhang, C.C. Tasan, M. Lai, A.-C. Dippel, D. Raabe, Complexion-mediated martensitic phase transformation in titanium, Nat. Commun. 8 (2017) 14210.
[6] X. Min, S. Emura, X. Chen, X. Zhou, K. Tsuzaki, K. Tsuchiya, Deformation microstructural evolution and strain hardening of differently oriented grains in twinning-induced plasticity β titanium alloy, Mater. Sci. Eng. A 659 (2016) 1–11.
[7] E. Bertrand, P. Castany, I. Péron, T. Gloriant, Twinning system selection in a metastable β-titanium alloy by Schmid factor analysis, Scr. Mater. 64 (12) (2011) 1110–1113.
[8] G.-H. Zhao, S.V. Ketov, J. Jiang, H. Mao, A. Borgenstam, D.V. Louzguine-Luzgin, New beta-type Ti-Fe-Sn-Nb alloys with superior mechanical strength, Mater. Sci. Eng. A 705 (2017) 348–351.
[9] X. Zhou, X. Min, S. Emura, K. Tsuchiya, Accommodative {332}⟨113⟩ primary and secondary twinning in a slightly deformed β-type Ti-Mo titanium alloy, Mater. Sci. Eng. A 684 (2017) 456–465.
[10] X. Zhou, X. Min, Effect of grain boundary angle on {332}⟨113⟩ twinning transfer behavior in β-type Ti–15Mo–5Zr alloy, J. Mater. Sci. 53 (11) (2018) 8604–8618.
[11] A. Crocker, Twinned martensite, Acta Metall. 10 (2) (1962) 113–122.
[12] H. Tobe, H.Y. Kim, T. Inamura, H. Hosoda, S. Miyazaki, Origin of {332} twinning in metastable β-Ti alloys, Acta Mater. 64 (2014) 345–355.
[13] M. Tane, T. Nakano, S. Kuramoto, M. Hara, M. Niinomi, N. Takesue, T. Yano, H. Nakajima, Low young's modulus in Ti–Nb–Ta–Zr–O alloys: cold working and oxygen effects, Acta Mater. 59 (18) (2011) 6975–6988.
[14] X. Min, K. Tsuzaki, S. Emura, K. Tsuchiya, Enhancement of uniform elongation in high strength Ti-Mo based alloys by combination of deformation modes, Mater. Sci. Eng. A 528 (13–14) (2011) 4569–4578.
[15] D.R. Steinmetz, T. Jäpel, B. Wietbrock, P. Eisenlohr, I. Gutierrez-Urrutia, A. Saeed-Akbari, T. Hickel, F. Roters, D. Raabe, Revealing the strain-hardening behavior of twinning-induced plasticity steels: theory, simulations, experiments, Acta Mater. 61 (2) (2013) 494–510.
[16] L. Remy, Kinetics of f.c.c. deformation twinning and its relationship to stress-strain behaviour, Acta Metall. 26 (3) (1978) 443–451.
[17] O. Bouaziz, N. Guelton, Modelling of TWIP effect on work-hardening, Mater. Sci. Eng. A 319 (2001) 246–249.
[18] O. Bouaziz, S. Allain, C. Scott, Effect of grain and twin boundaries on the hardening mechanisms of twinning-induced plasticity steels, Scr. Mater. 58 (6) (2008) 484–487.
[19] E.I. Galindo-Nava, P.E.J. Rivera-Díaz-del-Castillo, Understanding martensite and twin formation in austenitic steels: a model describing TRIP and TWIP effects, Acta Mater. 128 (2017) 120–134.
[20] B.C. De Cooman, Y. Estrin, S.K. Kim, Twinning-induced plasticity (TWIP) steels, Acta Mater. 142 (2018) 283–362.
[21] D. Kuroda, M. Niinomi, M. Morinaga, Y. Kato, T. Yashiro, Design and mechanical properties of new β-type titanium alloys for implant materials, Mater. Sci. Eng. A 243 (1–2) (1998) 244–249.
[22] M. Morinaga, Alloy design based on molecular orbital method, Mater. Trans. (2016) M2015418.
[23] X. Min, X. Chen, S. Emura, K. Tsuchiya, Mechanism of twinning-induced plasticity in β-type Ti-15Mo alloy, Scr. Mater. 69 (5) (2013) 393–396.
[24] X. Ji, S. Emura, X. Min, K. Tsuchiya, Strain-rate effect on work-hardening behavior in β-type Ti-10Mo-1Fe alloy with TWIP effect, Mater. Sci. Eng. A 707 (2017) 701–707.
[25] M. Oka, Y. Taniguchi, {332} Deformation twins in a Ti-15.5 pct V alloy, Metall. Trans. A. 10 (5) (1979) 651–653.
[26] W. Wang, X. Wang, W. Mei, J. Sun, Role of grain size in tensile behavior in twinning-induced plasticity β Ti-20V-2Nb-2Zr alloy, Mater. Charact. 120 (2016) 263–267.
[27] W. Wang, X. Zhang, J. Sun, Phase stability and tensile behavior of metastable β Ti-V-Fe and Ti-V-Fe-Al alloys, Mater. Charact. 142 (2018) 398–405.
[28] L. Ren, W. Xiao, C. Ma, R. Zheng, L. Zhou, Development of a high strength and high ductility near β-Ti alloy with twinning induced plasticity effect, Scr. Mater. 156 (2018) 47–50.
[29] S. Hanada, O. Izumi, Correlation of tensile properties, deformation modes, and phase stability in commercial β-phase titanium alloys, Metall. Trans. A. 18 (2) (1987) 265–271.
[30] H. Liu, M. Niinomi, M. Nakai, J. Hieda, K. Cho, Changeable young's modulus with large elongation-to-failure in β-type titanium alloys for spinal fixation applications, Scr. Mater. 82 (2014) 29–32.
[31] J. Gao, Y. Huang, D. Guan, A.J. Knowles, L. Ma, D. Dye, W.M. Rainforth, Deformation mechanisms in a metastable beta titanium twinning induced plasticity alloy with high yield strength and high strain hardening rate, Acta Mater. 152 (2018) 301–314.
[32] J. Zhang, F. Sun, Z. Chen, Y. Yang, B. Shen, J. Li, F. Prima, Strong and ductile beta Ti–18Zr–13Mo alloy with multimodal twinning, Mater. Res. Lett. 7 (6) (2019) 251–257.
[33] F. Sun, J. Zhang, M. Marteleur, T. Gloriant, P. Vermaut, D. Laillé, P. Castany, C. Curfs, P. Jacques, F. Prima, Investigation of early stage deformation mechanisms in a metastable β titanium alloy showing combined twinning-induced plasticity and transformation-induced plasticity effects, Acta Mater. 61 (17) (2013) 6406–6417.
[34] G.-H. Zhao, X. Liang, B. Kim, P.E.J. Rivera-Díaz-del-Castillo, Modelling strengthening mechanisms in beta-type Ti alloys, Mater. Sci. Eng. A 756 (2019) 156–160.
[35] G. Olson, M. Cohen, Kinetics of strain-induced martensitic nucleation, Metall. Trans. A 6 (4) (1975) 791.
[36] C. Sinclair, W. Poole, Y. Bréchet, A model for the grain size dependent work hardening of copper, Scr. Mater. 55 (8) (2006) 739–742.
[37] D. Hull, D.J. Bacon, Introduction to dislocations, Butterworth-Heinemann, 2001.
[38] R. Madec, B. Devincre, L. Kubin, From dislocation junctions to forest hardening, Phys. Rev. Lett. 89 (25) (2002) 255508.
[39] G.-H. Zhao, High-performance Load-bearing Alloys, KTH Royal Institute of Technology, 2017 Ph.D. thesis.
[40] M. Huang, P.E.J. Rivera-Díaz-del-Castillo, O. Bouaziz, S. Van Der Zwaag, Modelling strength and ductility of ultrafine grained BCC and FCC alloys using irreversible thermodynamics, Mater. Sci. Technol. 25 (7) (2009) 833–839.
[41] U. Kocks, H. Mecking, Physics and phenomenology of strain hardening: the FCC case, Prog. Mater. Sci. 48 (3) (2003) 171–273.
[42] A.P. Mouritz, Introduction to Aerospace Materials, Elsevier, 2012.
[43] S.J. McCormack, W. Wen, E.V. Pereloma, C.N. Tomé, A.A. Gazder, A.A. Saleh, On the first direct observation of de-twinning in a twinning-induced plasticity steel, Acta Mater. 156 (2018) 172–182.